Rotation–vibration spectra of icosahedral molecules. I. Icosahedral symmetry analysis and fine structure

William G. Harter and David E. Weeks
Los Alamos National Laboratory T-12, Los Alamos, New Mexico 87545
and Department of Physics, J. William Fulbright College of Arts and Sciences, University of Arkansas, Fayetteville, Arkansas 72701

(Received 4 August 1988; accepted 14 December 1988)

Icosahedral symmetry analysis is developed for analyzing eigensolutions of rovibrational tensor Hamiltonians for molecules such as $B_{12}H_{12}^{-2}$, $C_{20}H_{20}$, and C_{60}. Simplified asymptotic formulas and procedures are developed for obtaining rotational spectral fine structure for high angular momentum. $J = 100$ eigenlevels for sixth- and tenth-rank icosahedral tensors are discussed using different approximations and visualization schemes.

I. INTRODUCTION

Icosahedral symmetries I and $I_h = I \times C_i$ have become relevant for a number of physical, chemical and biological studies. Molecular structures known to have I_h symmetry include the borohydride anion[1,2] ($B_{12}H_{12}^{-2}$) and the recently synthesized dodecahedrane[3] ($C_{20}H_{20}$). More recently an I_h-symmetric structure has been proposed by Kroto *et al.*[4] for C_{60} carbon clusters. This structure has been named "Buckminster-Fullerene" or "Buckyball" after the inventor of the geodesic dome. Related but more complex I-symmetric structures have been established for meningitis, polio, and cold viruses.[5–7] Also, local icosahedral symmetry has been found in quasicrystalline solids.[8]

The icosahedral rotational symmetry group I or the full icosahedral rotation–reflection group $I_h = I \times C_i$ represent the symmetry of either the icosahedron or the dodecahedron which are two of the five platonic solids. The other platonic solids are the tetrahedron which has crystal point symmetry T_d and the hexahedron (cube) and octahedron which have octahedral crystal point symmetry $O_h = O \times C_i$. The $I(I_h)$ groups have 60(120) symmetry operations while T_d or O_h have only 24 or 48 operations, respectively. It can be shown[9] that icosahedral symmetry is the largest or highest finite symmetry in Euclidean 3-space. In this sense it is closest to spherical or R_3 symmetry. (Here we exclude the relatively trivial uniaxial or polygonal symmetries such as C_n groups which approximate cylindrical or R_2 symmetry as $n \to \infty$.)

The intent of this work will be to extend certain symmetry analysis methods to the study of spectral properties of icosahedrally symmetric molecules. The present paper will describe general aspects of icosahedral symmetry analysis and its application to rotational dynamics and spectral fine structure. We discuss spectral features which might be observed in any molecule or ion having I of I_h symmetry. Subsequent papers will use the icosahedral analysis to predict vibrational dynamics and spectral properties which depend upon the detailed structure of specific molecules. The harmonic rovibrational modes of a model for C_{60} will be discussed in the following paper, and the rovibrational modes of $C_{20}H_{20}$ and $B_{12}H_{12}^{-2}$ will be treated in later works.

We shall assume that some of the spectroscopic phenomenology[10–18] of tetrahedral or octahedral "spherical top" molecules can be generalized to the higher icosahedral symmetry species. At present there have been relatively few spectroscopic studies[2] of $B_{12}H_{12}^{-2}$ and no studies of $C_{20}H_{20}$ or C_{60}. For C_{60} one really needs spectroscopic evidence to establish the assumed icosahedral structure. Some predictions of infrared and raman spectral patterns based upon an icosahedral C_{60} model[19] will be given here and in the following paper. It is hoped that laser spectroscopic techniques which are successful in studies of octahedral molecules such as SF_6 or C_8H_8 can be applied as well to icosahedral molecules.

In particular, the rotational fine structure of infrared spectra of the octahedral molecules contains patterns which stand out very clearly even in the complicated bands of cubane[20] (C_8H_8). The theory of these fine-structure patterns as well as their underlying superfine structure has been developed for octahedral molecules.[16,18] Here we will extend this theory to icosahedral molecules in hopes that it may serve as a guide for high-resolution studies of these structures.

Fine-structure patterns may be useful for more than just "fingerprinting" the molecular spectra. As explained in Sec. III (and in previous works) the patterns are indicators of certain types of adiabatic rotational dynamics. They provide detailed information about the location and precessional dynamics of rotational momentum of the molecule as viewed in its rotating frame.[18] Rotational energy (RE) surfaces[17,18] will be used to map out the angular momentum phase portrait and to discuss the quantum mechanics and spectral properties of the molecular models. This will be important if any of the icosahedral molecules are to be used as "cages" to trap atoms or smaller molecules. Already, Smalley *et al.*[4] has shown evidence of trapped lanthanum (La) atoms in C_{60}. One may begin to speculate about the effects of a tiny "quantum lathe" around an excited atom or molecule in a vacuum or electromagnetic environment.

Also, the detailed rotational behavior is related to the vibrational dynamics through the coriolis interactions. The centrifugal distortion and anisotropic coriolis Hamiltonian of the molecule may be described in terms of tensor multipole expansions.[10,13,16] In the following sections (Secs. II and III) we shall discuss the icosahedral tensor Hamiltonians and show ways to understand their eigensolutions which are associated with the rotational spectral fine struc-

 0021-9606/89/094727-17$02.10

ture.[19] This will provide a context in which to introduce mathematical properties of the icosahedral symmetry representations which will be relevant for vibrational or electronic spectroscopy of these structures as well.

II. Icosahedral tensors

The correlation between angular momentum representations or J levels and the icosahedral irreducible representations (irreps) is given in Table I. As explained in Appendix A the icosahedral group I has five irreps labeled by $\alpha = A$, T_1, T_3, G and H of dimension $l^\alpha = 1, 3, 3, 4$, and 5, respectively. The numbers l^α give the degeneracy of the orbitals or "icosaharmonics" that would result in a quasi-crystal-field splitting of ordinary J orbitals or spherical harmonics Y^J_M belonging to a J level of degeneracy $2J+1$. The integer in the Jth row and αth column of Table I is the number of l^α-lets in any icosahedral splitting of a $(2J+1)$ multiplet.

One should note that $J = 0$, 1, and 2 levels are not split at all; they are merely "renamed" A, T_1, and H, respectively. The lowest J level to suffer icosahedral splitting is the $(J=3)$ septet which splits into a triplet (T_3) and quartet (G). (Note that we use the notation T_3 instead of T_2 for the second icosahedral triplet to indicate its $J=3$ character. In comparison, note that an *octahedral* field splits T_2 and E from $J=2$.) The first few rows of the correlation table provide some idea of the multipole character of the I irreps: A is scalar, T_1 is vector, or dipolelike, H is tensor or quadrupolelike, while T_3 and G are octupolelike.

The A column of the correlation table shows which multipole tensors can be icosahedral invariants and become part of icosahedral Hamiltonian. Besides the spherical scalar $(J=0)$ there are no nontrivial icosahedral tensors of rank less than six $(J=6)$. The two lowest rank tensors of rank six and ten will be discussed in this work.[21] The invariant sixth-rank tensor has the form

$$T^{[6]} = \frac{\sqrt{11}}{5} T^6_0 + \frac{\sqrt{7}}{5}(T^6_5 - T^6_{-5}), \tag{2.1}$$

while the tenth-rank invariant has the form

$$T^{[10]} = \frac{\sqrt{3\cdot 13\cdot 19}}{75} T^{10}_0 - \frac{\sqrt{11\cdot 19}}{25}(T^{10}_5 - T^{10}_{-5}) + \frac{\sqrt{3\cdot 11\cdot 17}}{75}(T^{10}_{10} + T^{10}_{-10}), \tag{2.2}$$

where the irreducible rth-rank tensors T^r_q transform under R_3 rotations $R(\alpha\beta\gamma)$ according to the standard Wigner D^r functions:

$$R(\alpha\beta\gamma) T^r_q R^\dagger(\alpha\beta\gamma) = \sum_p T^r_p D^r_{pq}(\alpha\beta\gamma). \tag{2.3}$$

A matrix element of an irreducible tensor in an angular momentum $|^J_K>$ basis is a product of a standard Clebsch–Gordan (CG) coefficient C^{rJJ}_{qKK}, and a reduced matrix element $\langle J\|r\|J\rangle$ according to the Wigner Eckart theorem:

$$\langle {}^{J'}_{K'}|T^r_q|{}^J_K\rangle = C^{rJJ'}_{qKK'}\langle J'\|r\|J\rangle. \tag{2.4}$$

A reduced matrix element is independent of the components q or K which label z components, but it may be a function of the total angular J quanta and the rank r. The reduced matrix factor depends upon the detailed physical definition of the states $|^J_K\rangle$ and the tensor operator T^r_q, while the many CG factors depend only on the geometry or angular anisotropy of the tensor operator. This factorization may allow one to study the possible forms of the spectral patterns without having detailed knowledge of the Hamiltonian and the molecular constants. In other words, similar patterns of energy levels can appear in pure rotational manifolds or in excited rovibronic manifolds. In fact the same patterns may appear in the spectra, as well, when selection rules allow transitions only between corresponding levels of each pattern.[17]

Rovibrational base states can have approximate vibronic (or vibrational) momentum l, pure (nuclear) rotor momentum N (this is often labeled R) and total angular momentum $J = l + N$. Dipole-active vibronic excited states have $l=1$ while initial states generally have $l=0$. Wave functions of definite l, N, and J can be constructed by coupling products of l and N wave functions:

$$\langle|[lN]^J_M(n)\rangle = \sum_{\substack{\lambda m \\ (M=\lambda+m)}} C^{lNJ}_{\lambda m M}\phi^l_\lambda(\text{vib}) r^N_{mn}(\text{rot}). \tag{2.5a}$$

Here $\phi^l_\lambda(\text{vib})$ is an angular vibronic (or vibrational) function defined in the laboratory fixed coordinates $\{xyz\}$ and $r^N_{mn}(\text{rot})$ is a rotor wave function

$$r^N_{mn}(\text{rot}) = D^N_{mn}(\alpha\beta\gamma)^*\sqrt{[N]}, \tag{2.5b}$$

where $[N] = 2N+1$, and D^N_{mn} is a Wigner D function. The quantum numbers m and n are components of N along lab-fixed axis z and body-fixed axis $\bar{z}$, respectively.

To compute molecular Hamiltonians it is convenient to reexpress (Eqs. 2.5) in terms of vibronic functions $\phi^l_\Lambda(\overline{\text{vib}})$ defined in molecule or body-fxed coordinates $\{\overline{xyz}\}$:

$$\phi^l_\Lambda(\overline{\text{vib}}) = \sum_\lambda \phi^l_\lambda(\text{vib}) D^l_{\lambda\Lambda}(\alpha\beta\gamma). \tag{2.6a}$$

By placing the inverse relation

TABLE I. Correlations between R_3 angular momentum J states ($J \leqslant 10$) and icosahedral symmetry species. (See Fig. 3 for more complete correlation and level splitting information.)

J	A	T_1	T_3	G	H
0	1	.	.	.	.
1	.	1	.	.	.
2	.	.	.	.	1
3	.	.	1	1	.
4	.	.	.	1	1
5	.	1	1	.	1
6	1	1	.	1	1
7	.	1	1	1	1
8	.	.	1	1	2
9	.	1	1	2	1
10	1	1	1	1	2

$$\phi^l_\lambda(\text{vib}) = \sum_\Lambda \phi^l_\Lambda(\overline{\text{vib}}) D^l_{\lambda\Lambda}(\alpha\beta\gamma)^* \tag{2.6b}$$

into Eq. (2.5a) and using standard Clebsch–Gordan relations,[16,18,22] we find

$$\begin{aligned}\langle|[lN]^J_M(n)\rangle &= \sum_{\substack{\Lambda,k \\ (K-\Lambda=n)}} C^{lNJ}_{\Lambda nK}([N]/[J])^{1/2}\phi^l_\Lambda(\overline{\text{vib}}) r^J_{MK} \\ &= (-1)^{N-J} \sum_{\substack{\Lambda,K \\ (\Lambda+K=n)}} C^{lJN}_{\Lambda Kn}(-1)^\Lambda \phi^l_{-\Lambda}(\overline{\text{vib}}) r^J_{MK} \\ &= (-1)^{N-J} \sum_{\substack{\Lambda,K \\ (\Lambda+K=n)}} C^{lJN}_{\Lambda Kn}\phi^{*l}_\Lambda(\overline{\text{vib}}) r^J_{MK}. \end{aligned} \tag{2.7}$$

This coupling "substracts" l from J to give N and the resulting state without the phase $(-1)^{N-J}$ will be written as follows[22]:

$$\langle|[lJ]^N_n(m)\rangle = \sum_{\Lambda,K} C^{lJN}_{\Lambda Kn}\phi^{*l}_\Lambda(\overline{\text{vib}}) r^J_{MK}. \tag{2.8}$$

The molecular Hamiltonian will be composed of scalar and tensor parts:

$$H = H_{\text{scalar}} + H_{\text{tensor}}. \tag{2.9a}$$

The scalar part

$$H_{\text{scalar}} = \nu_{\text{vib}} + BJ^2 + DJ^4 + \cdots - 2B\,\mathbf{J}\cdot\mathbf{l}. \tag{2.9b}$$

contains the vibronic or vibrational energy ν_{vib}, the rigid spherical rotor energy BJ^2, isotropic distortion energies such as DJ^4, and the first-order isotropic Coriolis interaction interaction $-2B\,\mathbf{J}\cdot\mathbf{l}$. The latter splits the excited state levels belonging to different $N = J-1, J$, and $J+1$ for each J, but scalar operators cannot split the $(2N+1)$-fold degeneracy of the angular momentum levels.

The tensor part of the Hamiltonian which is responsible for rotational level fine-structure splitting has the form

$$\begin{aligned} H_{\text{tensor}} &= \sum_{r_1r_2r_3} t_{r_1r_2r_3} T^{[r_3]}[r_1,r_2] \\ &= \sum_{r_1r_2}\{t_{r_1r_26}T^{[6]}[r_1,r_2] + t_{r_1r_210}T^{[10]}[r_1,r_2] + \cdots\}, \end{aligned} \tag{2.9c}$$

where Hecht's[10] notation t_{pqr} is used for the molecular tensor constants, and $T^{[6]}$ or $T^{[10]}$ denote icosahedral tensors of the form (2.1) or (2.2), respectively with each T^r_q replaced by a tensor product:

$$\begin{aligned} T^r_q[r_1,r_2] &= [T^{r_1}(\overline{\text{vib}}) \times T^{r_2}(\overline{\text{rot}})]^r_q \\ &= \sum_{\substack{q_1q_2 \\ (q_1+q_2=q)}} C^{r_1r_2r}_{q_1q_2q} T^{r_1}_{q_1}(\overline{\text{vib}}) T^{r_2}_{q_2}(\overline{\text{rot}}). \end{aligned} \tag{2.9d}$$

Here $T^{r_1}_{q_1}(\overline{\text{vib}})$ is a rank-r_1 tensor which acts on the internal vibronic or vibrational wave function $\phi^{*l}_\Lambda(\overline{\text{vib}})$, and $T^{r_2}_{q_2}(\text{rot})$ is a rank-r_2 tensor which affects the J and internal K quanta of the rotor wave function r^J_{MK} in Eq. (2.8). [Lab-defined operators which affect the external M quanta are more easily evaluated using the original form (2.5a) of the basis.[16]]

The scalar matrix elements are easily evaluated since they are diagonal in the $|[lJ]^N_n(M)\rangle$ basis

$$\begin{aligned}\langle[l'J']^{N'}_{n'}(M')|H_{\text{scalar}}|[lJ]^N_n(M)\rangle &= \delta^{l'l}\delta^{J'J}\delta^{N'N}\delta_{n'n}\delta_{M'M} \\ &\times\{\langle\nu_{\text{vib}}\rangle + BJ(J+1) + D[J(J+1)]^2 \\ &+ \cdots - B\zeta[J(J+1) - N(N+1) + l(l+1)]\}, \end{aligned} \tag{2.10a}$$

where

$$N = J+l, J+l-1, \ldots, |J-l|. \tag{2.10b}$$

For vibronically unexcited levels one has $l=0$ and $J=N$, and there is no contribution from the Coriolis term.

The tensor matrix elements are evaluated using the Wigner Eckart theorem as before for each component (2.9d) of (2.9c):

$$\begin{aligned}\langle[l'J']^{N'}_{n'}|[T^{r_1}(\overline{\text{vib}}) \times T^{r_2}(\overline{\text{rot}})]^r_q|[lJ]^N_n\rangle &= C^{rNN'}_{qnn'}\langle[l'J']N'\|[r_1r_2]^r\|[lJ]N\rangle. \end{aligned} \tag{2.11a}$$

The reduced matrix element is then evaluated using Racah recoupling algebra into a product of vibronic and rotational reduced matrix elements:

$$\begin{aligned}\langle[l'J']N'\|[r_1r_2]^r\|[lJ]N\rangle &= ([N'][r][N])^{1/2}\begin{Bmatrix} l' & l & r \\ J' & J & r_2 \\ N' & N & r \end{Bmatrix} \\ &\times\langle l'\|r_1\|l\rangle_{\text{vib}}\langle J'\|r_2\|J\rangle_{\text{rot}}. \end{aligned} \tag{2.11b}$$

The vibronic reduced matrix element can be treated as a constant since it is independent of J of N. The rotational reduced matrix can be evaluated using Racah algebra[16,23] while asuming a convenient form for $T^r(\overline{\text{rot}})$:

$$\begin{aligned}\langle J'\|r\|J\rangle_{\text{rot}} &= \delta^{J'J}[(2J+r+1)!/(2J-r)!(2J+1)]^{1/2}/2^r. \end{aligned} \tag{2.12}$$

The form has been chosen so that $\langle J\|1\|J\rangle = \sqrt{J(J+1)}$ and $\langle J\|r\|J\rangle \to J^r$ as $J\to\infty$.

The Racah formulas show that the fine-structure tensor splitting patterns vary as some high power of j or N. In the vibronically unexcited states ($l=0$, $N=J$) the splitting pattern width due to $T^{[6]}$ and $T^{[10]}$ would be proportional to $t_{066}J^6$ and $t_{01010}J^{10}$, respectively, while for a dipole active excited state ($l=1$, $N=J\pm1, J$) the splitting would vary according to a combination of $J^2, J^4, \ldots$, and J^{10} depending on the values of tensor constants t_{pqr}. By comparison the Coriolis splittings vary according to the Landé interval rule and are linear in J. However, one should expect the Coriolis constant $B\zeta$ to be much larger than the tensor constants. In SF_6, for example, $2B(1-\zeta_4) = 6.6\times10^9$ Hz is the splitting between neighboring P and R lines while the ν_4 tensor constants $t_{044} = 5.7$ Hz and $t_{224} = -6.4\times10^5$ Hz yield a $J=88$ fine-structure pattern which is about 3.7×10^9 Hz wide. (See, for example, Figs. 1, 3, and 7 of Ref. 17).

We shall discuss the icosahedral tensor fine-structure patterns which result when we can ignore mixing between different Coriolis components $N = J+l, \ldots, |J-l|$ with the

same J. Mixing effects are complicated and have been studied so far only in ($l=1$) models of certain octahedral tensors.[18,22] Without knowing the icosahedral molecular constants $B\zeta$ and t_{pqr} one cannot be sure that ignoring off-diagonal ($N \neq N$) components is a useful approximation. Nevertheless, it does seem likely that the icosahedral t_{pqr} constants are even smaller than they are in SF_6 due to the high symmetry, while scalar Coriolis constants $B\zeta$ are probably about the same as SF_6 values. It is even possible that t_{pqr} are practically zero and that all icosahedral molecules are really spherical tops. However, the icosahedral molecules are all cage molecules and they have greater inertia and higher J values. Therefore one should expect the anisotropic distortion effects to eventually show up in spectral fine structure.

III. SIXTH-RANK ICOSAHEDRAL TENSOR EIGENSOLUTIONS

We consider now the structure of eigensolutions of icosahedral tensor Hamiltonians and ways to understand their structure. The simplest possible tensor Hamiltonian involving a rigid spherical rotor term and the sixth-rank tensor (2.1) will be discussed first:

$$H = BJ^2 + t_{066}T^{[6]}. \tag{3.1}$$

An example of eigenvalues and their corresponding levels for $J=100$ is shown in Fig. 1. These values are plotted for the Hamiltonian (3.1) with $B=0$ and the tensor constant and reduced matrix element set to unity ($t_{066}=1.0$, $\langle 100\|6\|100\rangle = 1.0$).

The matrix which was diagonalized to give Fig. 1 is a 201-dimensional representation of the sixth-rank tensor $T^{[6]}$ in Eq. (2.1) as given by the Wigner Eckart theorem (2.4). Exact numerical diagonalization of this matrix may be simplified by icosahedral symmetry projection methods so that extremely high J values of, say, 500 or 1000 could be handled on a microcomputer such as a MacIntosh 512K. (These procedures are described in Appendix B.) Since the B value for C_{60} is about 30 times greater than for SF_6 one expects to observe J values of several hundred quanta for C_{60} at room temperature. However, for this discussion we shall consider "low" J values ($J \leqslant 120$) which can be solved with high accuracy relatively easily without the aid of symmetry projection on a mainframe computer such as a CDC-7600 or CRAY-1. The objective of the following discussion is to develop quick asymptotic high-J approximations which simplify computation and analysis of eigensolutions and provide physical interpretations of them.

Icosahedral symmetry representations A, T_1, T_3, G, and H are used to label the levels in Fig. 1 of degeneracy 1, 3, 3, 4, and 5, respectively. However, most of the levels are crowded into quasidegenerate clusters of these species. The top ten or so clusters have a quasidegeneracy of 12, while the two or three lowest clusters each contain 20 levels. The degree of quasidegeneracy varies over many orders of magnitude. For example, the top cluster contains four species A, T_1, H and T_3 whose energies are equal to nearly 12 significant figures. In contrast, the 11th highest cluster contains an identical set of species whose energies differ already in the second or third significant figures.

The splitting within clusters is called *superfine* structure while the splitting between clusters is called *fine*-structure splitting. Each kind of splitting can be associated with a separate mechanism or dynamics.[14–18] One should note that the superfine splitting decreases quasiexponentially as the energy ranges above or below the neighborhood of -0.2 in Fig. 1. (This neighborhood is labeled the separatrix region in the figure for reasons that will be explained shortly.) Note also that the *fine*-structure splitting *increases* noticeably while going away from the separatrix region.

A convenient picture of a tensor eigenvalue spectrum can be obtained using the rotational energy (RE) surface shown in Fig. 2. The RE surface function of a tensor Hamiltonian is obtained by replacing each tensor component T^r_q by a Wigner D-function expression which depends on the direction of the angular momentum vector $\mathbf{J}$ in the molecular frame:

$$T^r_q(\mathbf{J}) = D^r_{0q}(\cdot,\beta,\gamma)|J|^r = D^{r*}_{q0}(-\gamma,-\beta,0)|J|^r \tag{3.2a}$$

$$= (4\pi/[r])^{1/2}Y^r_q(-\beta,-\gamma)|J|^r, \tag{3.2b}$$

where

$$|J| = [J(J+1)]^{1/2} \tag{3.2c}$$

is the quantum magnitude of $\mathbf{J}$ and $Y^r_q(\theta,\phi)$ is a standard spherical harmonic. The direction of $\mathbf{J}$ is classically defined in the molecular body frame $\{\overline{xyz}\}$ by a polar angle $(-\beta)$ and an azimuthal angle $(-\gamma)$:

$$\begin{aligned} J_{\bar{x}} &= |J|\sin(-\beta)\cos(-\gamma), \\ J_{\bar{y}} &= |J|\sin(-\beta)\sin(-\gamma), \\ J_{\bar{z}} &= |J|\cos(-\beta). \end{aligned} \tag{3.3}$$

Since $\mathbf{J}$ is lab-fixed for a free rotor one may let it define the lab z axis. Then the angles β and γ are the second and third Euler angles. (The first Euler angle α is ignorable since lab-defined z-component $\langle J_z\rangle = M$ is a constant of the motion.) The RE surface determines allowed classical trajectories in β and γ coordinates as explained below.

The surface in Fig. 2 is given by the following radial function for the sixth-rank Hamiltonian (3.1) and (2.1):

$$\mathrm{RE}(\beta,\gamma) = B|J|^2 + t_{066}\left\{\frac{\sqrt{11}}{5}D^6_{0,0}(\cdot,\beta,\gamma) + \frac{\sqrt{7}}{5} \times [D^6_{0,5}(\cdot,\beta,\gamma) + D^6_{0,-5}(\cdot,\beta,\gamma)]\right\}|J|^6 \tag{3.4a}$$

$$= B|J|^2 + t_{066}\frac{\sqrt{11}}{80}(231\cos^6\beta - 315\cos^4\beta + 105\cos^2\beta - 5) + 42\cos\beta\sin^5\beta\cos \times\gamma(16\cos^4\gamma - 20\cos^2\gamma + 5)|J|^6. \tag{3.4b}$$

The surface represents a radial plot of the rotational energy as a function of the direction (β,γ) of the angular momentum vector $\mathbf{J}$ in the molecular frame for fixed magnitude $|\mathbf{J}|$.

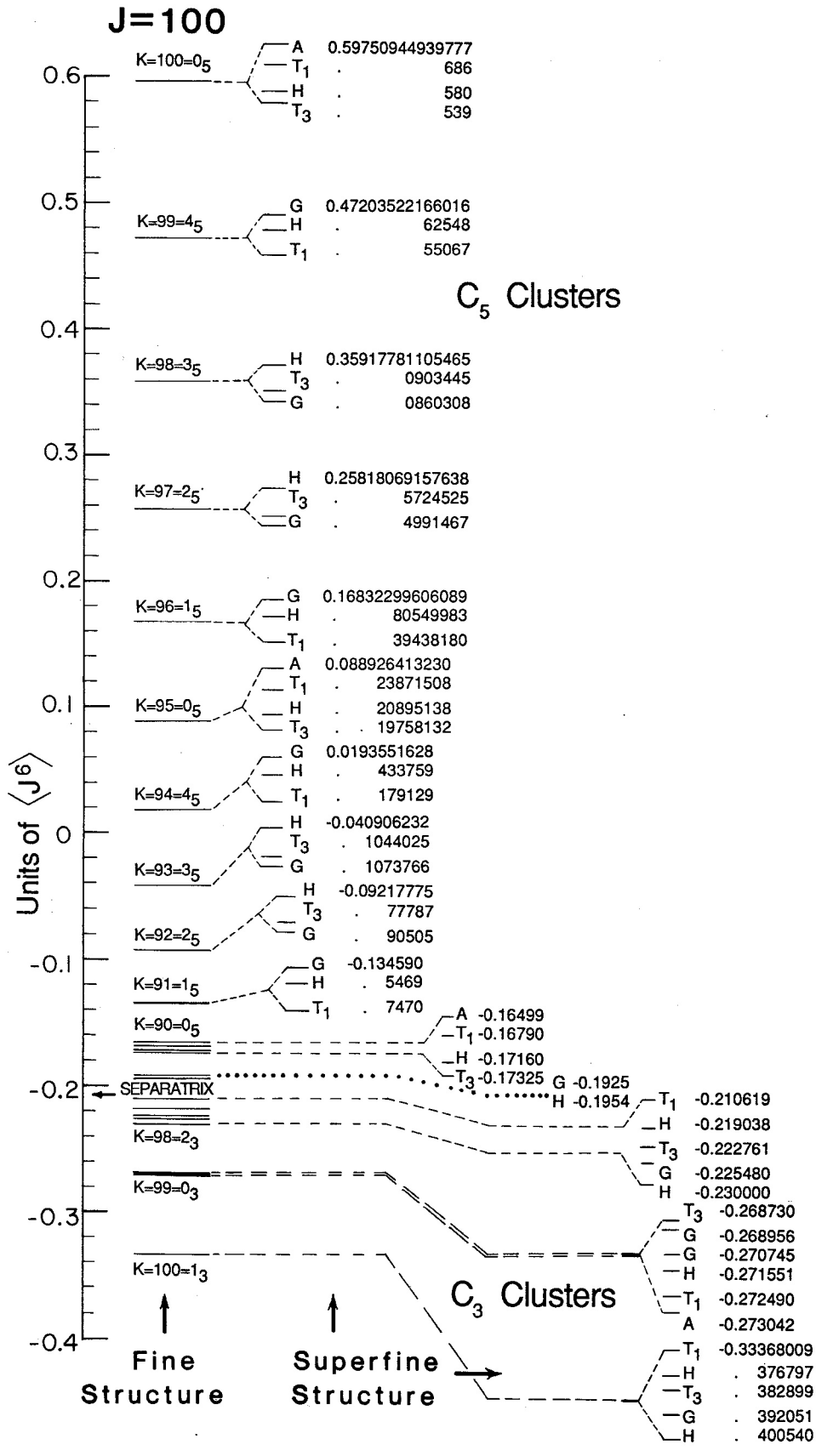

FIG. 1. Eigenvalue spectrum with $J = 100$ for sixth-rank icosahedral tensor Hamiltonian $T^{(6)}$. (After Ref. 19) Superfine-structure splittings are indicated numerically by displaying the significant digits which differ for different species in a cluster. The graphical displays of the level splittings are greatly exaggerated.

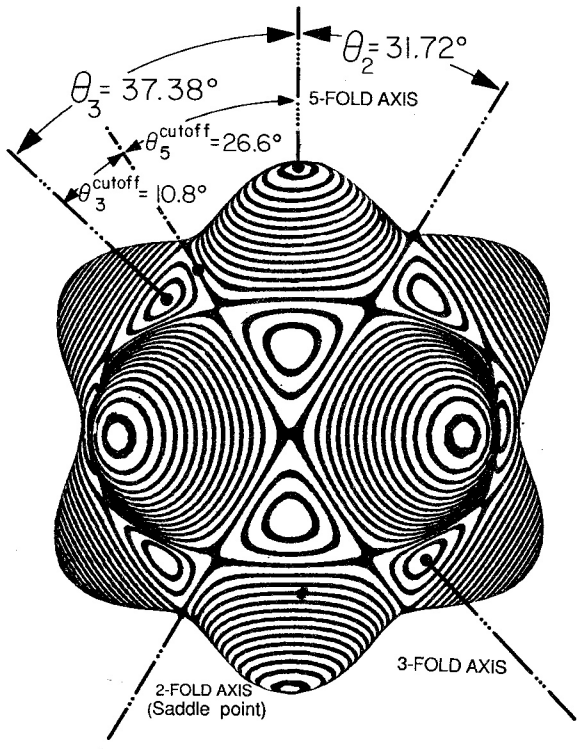

FIG. 2. Rotational energy (RE) surface for the sixth-rank icosahedral tensor Hamiltonian. (After Ref. 19) Trajectories or contours on the 12 fivefold symmetric hills correspond to clusters of 12 levels in Fig. 1, and the contours on the 20 threefold symmetry valleys correspond to the clusters of 20 levels. Angles between key symmmetry axes can be used to compute the energy and number of each type of level pattern.

The surface in Fig. 2 is drawn for $|J| = 1$, and constants $B = 1.0$ and $t_{066} = 0.2$ were chosen arbitrarily. Different choices for B and t_{066} do not affect the *eigenvectors* of the Hamiltonian (3.1). They only affect the overall scaling for the eigenvalues while the form of the splitting patterns is unchanged.

The form of the fine-structure splitting patterns in Fig. 1 is found by inspecting the RE surface in Fig. 2. The clusters of levels in Fig. 1 can be related to certain classical trajectory paths in Fig. 2. Allowed classical paths of the J vector are simply level curves or topography lines of constant energy which are drawn in Fig. 2. Most of the lines surround pentagonal or C_5 symmetric peaks on the surface. It is this type of trajectory, appropriately quantized, that is associated with each of the 12-fold quasidegenerate clusters which account for most of the levels in Fig. 1. There is a 12-fold degeneracy for each of these clusters because there are 12 equivalent C_5-symmetric peaks. The 20-fold quasidegenerate clusters in the lower portion of Fig. 1 are each associated with 20 equivalent triangular or C_3-symmetric trajectories at an energy level in the valleys of the RE surface.

The division between the different C_3 and C_5 symmetry regions is marked by separatrix curves or separatrices which are intersecting great circles. Their intersections occur at 30 different C_2-symmetric axes which are unstable saddle points on the RE surface. One of the saddle points occurs at $\theta_2 = -\beta_2 = 31.72°$ and $\phi_2 = -\gamma_2 = 180°$. Substitution into Eq. (3.4b) gives the separatrix energy of

$$\mathrm{RE}(\beta_2,\gamma_2) = B|J|^2 - \tfrac{1}{16}\sqrt{11}\,t_{066}|J|^6. \tag{3.5}$$

The value $-\frac{1}{16}\sqrt{11} = -0.207$ is labeled "*separatrix*" in Fig. 1. This is where the levels are least clustered. By contrast the clusters are very tight near the C_5 axis at $\theta_5 = 0$ and $\phi_5 = 0$ and the C_3 axis at $\theta_3 = -\beta_3 = 37.38°$ and $\phi_3 = 0$. These points give the upper and lower bounds, respectively, to the energy spectrum in Fig. 1:

$$\mathrm{RE}(\beta_5,\gamma_5) = B|J|^2 + \tfrac{1}{5}\sqrt{11}\,t_{066}|J|^6, \tag{3.6a}$$

$$\mathrm{RE}(\beta_3,\gamma_3) = B|J|^2 - \tfrac{1}{9}\sqrt{11}\,t_{066}|J|^6. \tag{3.6b}$$

The values

$$\tfrac{1}{5}\sqrt{11}: -\tfrac{1}{16}\sqrt{11}: -\tfrac{1}{9}\sqrt{11} = 0.663: -0.207: -0.369 \tag{3.6c}$$

determine the ratio of classical (maximum:separatrix:minimum) energies in units of $t_{066}|J|^6$ relative to the J-multiplet center of gravity. As J becomes much larger the highest C_5 cluster eigenvalues will approach 0.66 (for $J = 100$ it is only 0.59), and the lowest C_3 cluster will approach -0.36 (for $J = 100$ it is -0.33).

The int*ra*cluster or superfine-structure splitting decreases rapidly for energies that are farther from the separatrix. The splitting is proportional to the rate of a tunneling process which involves evanescent waves extending across the saddle points. Numerical evaluation of these tunneling rates by saddle path integration gives good approximations to superfine splittings in octahedral RE surface models.[14(e),18] A discussion of icosahedral cluster splitting will be given in Sec. IV.

The intercluster or fine-structure splitting in Fig. 1 is approximately proportional to the rate of motion of the J vector around the level curve trajectory paths in Fig. 2.[14(e),18] One can visualize this motion as a precession of the rotation axis or a "rotation of rotation." One expects the precessional motion to be much slower than the rotational motion but (usually) much faster than tunneling. Pure rotational angular frequency is given by $\omega = 2B|J|$ which is also the splitting between different pure rotational J levels. The precessional frequency, on the other hand, is proportional to the splitting between different K levels within each J manifold, that is, to the fine-structure splitting between neighboring clusters. This, in turn, is much greater than the superfine-structure splitting if a separatrix is not nearby. Superfine-structure splitting is proportional to a tunneling rate. In the separatrix region tunneling and precessional motions appear to be indistinguishable and clusters are badly split up.

One of the keys to understanding cluster structure and dynamics involves the assignment of K-quantum values to each cluster and to their corresponding semiclassical trajectories on the RE surface. Generally, K is taken to be the projection of J on a body $\bar{z}$ axis. The difference here is that one may use several $\bar{z}$ axes; one for each hill and valley of an RE surface. In Fig. 2 we imagine 12 equivalent $\bar{z}_5$ axes, 20 equivalent $\bar{z}_3$ axes. Prototypical $\bar{z}_3$ and $\bar{z}_5$ axes are indicated by lines with 3 and 5 dots, respectively, in Fig. 2. In this way we obtain an overcomplete set of bases. However, only a few of the largest K states are actually used. For example, Fig. 1

shows that only the $K = 100$, 99, and 98 clusters appear below the separatrix. Each of these three clusters belongs to a path surrounding one of 20 z_3 axes and together they account for 60 of the 201 levels for $J = 100$. Another 132 levels above the separatrix belong to 11 clusters labeled by $K = 100$, 99, ..., 89, and 90, respectively, which are each associated with 12 $\bar{z}_5$ axes. The remaining nine levels belong to the G and H species just above the separatrix which are not obviously part of any cluster.

A. Semiclassical approximations

There are simple procedures for predicting the approximate energies and lengths of each K sequence of clusters using the RE surface geometry. These are based upon the use of simple angular momentum cones which characterize the fundamental angular uncertainty relations. The quantum angular momentum eignevalues

$$J_{\bar{z}}|^J_K\rangle = K|^J_K\rangle, \tag{3.7a}$$

$$J^2|^J_K\rangle = [J(J+1)]|^J_K\rangle, \tag{3.7b}$$

suggest that the "quantum locus" of the J vector for each $|^J_K\rangle$ state is a cone. The altitude of the cone represents the $\bar{z}$ projection of $\mathbf{J}$ which is K by Eq. (3.7a), while the slant height represents the quantum magnitude (3.2c) which is $|J| \equiv [J(J+1)]^{1/2} \sim J + \frac{1}{2}$ by Eq. (3.7b). The apex half-angle θ^J_K of the cone is a measure of the angular uncertainty of the $|^J_K\rangle$ state, where

$$\cos\theta^J_K = K/[J(J+1)]^{1/2} \equiv K/|J|. \tag{3.8}$$

The states with the highest possible K values, namely, $K = J, J-1, \ldots$ are the ones with the narrowest cones and so they have minimum uncertainty. These are the ones that appear nearest to the extreme values [Eq. (3.6c)] of the classical RE surface. Furthermore, one may approximate the highest energy eigenvalues by substituting the apex angle $\theta^J_K = -\beta$ from Eq. (3.8) into the RE surface expression (3.4b). For example, substituting $\cos\theta^{100}_{100} = 0.9950$ into Eq. (3.4b) yields an energy of 0.596 which agrees well with the highest eigenvalue 0.5975 given in Fig. 1. This approximation shows that the extreme energy levels correspond to semiclassical trajectories which lie on or very near to angular momentum cone intersections with the Re surface. The difference between the classical limiting value (0.663) in Eq. (3.6c) and the highest eignevalue (0.596) might well be called the "angular zero-point" energy.

The cone approximation is consistent with an asymptotic relation[24] between Legendre harmonic functions and the diagonal CG coefficients in the $K = K'$ matrix elements of tensor operators T^r_0 given by the Wigner Eckart theorem (2.4). The approximation is given in the second line below

$$\langle^J_K|T^r_0|^J_K\rangle = C^{rJJ}_{0KK}\langle J\|r\|J\rangle$$

$$\simeq D^r_{00}(\cdot\theta^J_K\cdot)|J|^r \quad (\text{for } J \gg 1), \tag{3.9}$$

where

$$D^r_{00}(\cdot\theta\cdot) = P_r(\cos\theta)$$

is a Wigner–Legendre polynomial and cone angle θ^J_K is given by Eq. (3.8).

These approximations are less accurate for K values whose energies approach the separatrix region. However, they can often be used to estimate the K cutoff values which mark the end of a given K series of clusters. These are the values for which the θ^J_K cones reach the separatrix. According to Fig. 2 the separatrices subtend an angle $\theta^{\text{cutoff}}_3 = 10.8°$ and $\theta^{\text{cutoff}}_5 = 26.6°$ with threefold and fivefold axes, respectively. Therefore the K-cutoff values are

$$K^{\text{cutoff}}_3 = \sqrt{J(J+1)}\cos 10.8° = 98.7 \quad (\text{for } J = 100),$$

$$K^{\text{cutoff}}_5 = \sqrt{J(J+1)}\cos 26.6° = 89.8. \tag{3.10}$$

These give approximately the lowest K values observed in Fig. 1.

The paths farthest from a separatrix and closest to a maximum or minimum point on the RE surface are the ones with the most nearly circular shape. They most nearly conserve the projection $\langle J_z\rangle = K$ of angular momentum onto their local $\bar{z}$ axis of quantization. Their corresponding quantum energies are given most accurately by the diagonal tensor components T^r_0 of a Hamiltonian which is represented in a basis that has this $\bar{z}$ axis. As the energy approaches a separatrix the off-diagonal components $T^r_q (q \neq 0)$ begin to take effect. They reduce the classical RE surface path symmetry from circular to a C_q-symmetric star, and they perturbatively mix quantum states of definite K with ones that have $K' = K \pm q$.

A semiclassical path integral calculation[14(e),18] of energies redefines K. There K is an integer that results from picking the energy that quantizes the angular path action integral around the C_q-symmetric path:

$$K = \left(\int_0^{2\pi} J_{\bar{z}}\, d\gamma\right)/h. \tag{3.11}$$

This gives reasonably accurate energy values (and exactly integral K values). In a sense, the K nonconservation gets averaged out. Path integrals and wavepacket propagation methods[25,26] on general RE surfaces will be discussed in future works.

B. Semiquantum approximations

Another approximation which is usually more accurate, and in this case more convenient, involves a perturbation expansion in the local C_q axial basis. For the C_5 cluster energies one obtains

$$H^{(2)}(K) = H_1(K) + H_2(K)$$

$$= H_1(K) + \frac{|V_5(-K)|^2}{H_1(K) - H_1(K+5)}$$

$$+ \frac{|V_5(K)|^2}{H_1(k) - H_1(K-5)}, \tag{3.12a}$$

where the first-order approximation involves only diagonal matrix elements

$$H_1(K) = \frac{\sqrt{11}}{5} t_{066}\langle^J_K|T^6_0|^J_K\rangle$$

$$= \frac{\sqrt{11}}{5} t_{066} C^{6JJ}_{0KK}, \tag{3.12b}$$

and the second-order corrections involve matrix elements that are five steps off the diagonal:

$$V_5(K) = \frac{\sqrt{7}}{5} t_{066} \langle {}^{J}_{K-5} | T^6_{-5} | {}^{J}_{K} \rangle = \frac{\sqrt{7}}{5} t_{066} C^{6JJ}_{-5KK-5}.$$

The reduced matrix element $\langle J \| 6 \| J \rangle \sim |J|^6$ has been set to unity above. The CG coefficients can be expressed as polynomials

$$C^{6JJ}_{0KK} = (2J+1)^{1/2} \frac{-20(J+3:-2) + 84K^2(5J^4+10J^3-25J+14) - 420K^4(3J^2+3J-7) + 924K^6}{(2J+7:-5)^{1/2}}, \tag{3.13a}$$

$$C^{6JJ}_{5KK+5} = \frac{-(2K+5)}{5!} \left(\frac{11!(2J+1)(J+K+5:1)(J-M+0:-4)}{(25+7:-5)} \right)^{1/2} = C^{6JJ}_{5-K-K-5}. \tag{3.13b}$$

The expressions with colons represent partial factorials

$$(X+n:m) = (X+n)(X+n-1)(\cdots)(X+m)$$
$$= (X+n)!/(X+m-1)! \tag{3.13c}$$

A comparison is given between the various approximations to $J = 100$ eigenvalues for C_5 clusters in Table II. One should note that the errors of the second-order approximations are often less than the amount of superfine splitting. This amounts to nine or ten significant figures for $K = 100$ and about five figures for $K = 95$. (The exact values used in Table II are the level averages or cluster centers of gravity for K levels quoted in Fig. 1.) The first-order approximations are quicker but not quite as accurate. H_1 gives five-figure accuracy for $K = 100$ and three-figure accuracy for $K = 95$. The cone approximation is accurate to about two significant figures throughout the C_5 manifold.

The same methods can be applied to any C_q system of clusters. It is only necessary that the tensor operator be expressed in a basis which includes the local C_q symmetry axis as the $\bar{z}$ axis of quantization. The cone and first-order approximations depend only on the coefficients involving the diagonal matrix elements T^r_0 and not on the off-diagonal perturbations of $T^r_{\pm q}$, and so forth. For the C_3 system of clusters one can quickly determine the diagonal operator to be $-(\sqrt{11}/9)T^6_0$ from Eq. (3.6). This means the C_3 cluster approximations for $K = 100$, 98, and 99, are approximately the corresponding C_5 approximations multiplied by a factor of $-5/9$.

C. Superfine structure

None of the approximations given so far begin to explain the rich symmetry structure contained within each K cluster in Fig. 1. It is important to know which icosahedral symmetry species A through H contribute to each quasidegenerate cluster of 12 or 20 levels in Fig. 1 or in 30 or more levels which show up in more complex tensor spectra. Also, the relative ordering and spacing of levels in a cluster is indicative of long time dynamics and may be of interest for high-resolution spectroscopy.[17,18,26]

The key to cluster symmetry involves correlations between local C_q symmetry of the RE surface topography and global icosahedral symmetry of the entire surface. The correlation tables between local subgroups C_2, C_3, and C_5 of I are given in Table III.

The rows of these tables list the C_q species that would split from each icosahedral species under a C_q-symmetric perturbation such as a Zeeman splitting. For example, T_1 splits into three levels 1_3, 0_3, and $2_3 = -1_3$ under a C_3 perturbation. This corresponds to an ordinary external or "applied" symmetry breaking in which the Hamiltonian is artificially reduced in symmetry. Then the levels belonging to global symmetry species *split* into levels belonging to local symmetry species.

The columns of these tables list the I species which are contained in clusters such as the ones found in Fig. 1. For example, the first column of the C_5 table lists the first cluster (AT_1T_3H) seen at the top of Fig. 1. This corresponds to an

TABLE II. Comparison of exact cluster level center of gravity and approximations for C_5 clusters in $J = 100$ eigenvalues of Fig. 1.

K	Exact values	Cone values[a]	First order[b]	Second order[c]
100	0.597 509 4494	0.595 892	0.597 508 961 164	0.597 509 449 335
99	0.472 035 2216	0.470 622	0.472 032 079 319	0.472 035 220 753
98	0.359 177 8095	0.357 945	0.359 165 939 371	0.359 177 802 957
97	0.258 180 6662	0.257 100	0.258 146 253 917	0.258 180 630 023
96	0.168 322 7319	0.167 351	0.168 237 832 860	0.168 322 579 103
95	0.088 922 7345	0.087 993	0.088 733 929 942	0.088 921 014 675
94	0.019 338 8172	0.018 348	0.018 955 569 610	0.019 337 711 681
93	−0.041 008 007 .	−0.042 236	−0.041 748 957 791	−0.041 009 456 076
92	−0.092 620 22 . .	−0.094 383	−0.094 004 998 626	−0.092 622 350 440
91	−0.135 843	−0.138 692	−0.134 118 967 94	−0.135 868 735 094
90	−0.169 435	−0.175 736	−0.175 543 735 626	−0.170 848 179 938

[a] Semiclassical cone values are obtained using approximations (3.4) and (3.8) with $\beta = \theta^J_K$ and $\gamma = 0$.
[b] Semiquantum approximate values are obtained using Eq. (3.12). The first-order (H_1) results are given.
[c] Semiquantum approximate values are obtained using Eq. (3.12). The second-order (H_2) results are given.

TABLE III. Correlations between local cyclic rotational subgroup representations and global icosahedral symmetry representations. Cyclic species notation p_q is read as p mod q.

C_2	O_2	1_2	C_3	0_3	1_3	$2_3=-1_3$	C_5	0_5	1_5	2_5	$3_5=-2_5$	$4_5=-1_5$
A	1	.	A	1	.	.	A	1	.	.	.	.
T_1	1	2	T_1	1	1	1	T_1	1	1	.	.	1
T_3	1	2	T_3	1	1	1	T_3	1	.	1	1	.
G	2	2	G	2	1	1	G	.	1	1	1	1
H	3	2	H	1	2	2	H	1	1	1	1	1

internal or "spontaneous" symmetry breaking in which the wave functions become isolated into separate but equivalent local symmetry domains. Then the levels belonging to global symmetry species *cluster* or "unsplit" as a result of small tunneling between the domains which contain copies of a given local symmetry wave function.

The first column in the C_5 table is labeled 0_5 which means that it belongs to a representation with zero quanta modulo five (0 mod 5). The clusters labeled by integers $K=100$, 95, and 90, i.e., $K=0$-mod-5, all contain the same species that appear in an induced representation

$$0_5\uparrow I = A + T_1 + T_3 + H.$$

The next induced representation in Table III is

$$1_5\uparrow I = T_1 + G + H$$

and it labels the clusters with $K=96$ and 91 in Fig. 1. They have the same structure as the $-1_5=4_5$ clusters with $K=99$ and 94. Finally the induced representations

$$2_5\uparrow I = T_3 + G + H = -2_5\uparrow I \equiv 3_5\uparrow I$$

label the remaining $K=98$, 97, 93, and 92 clusters in Fig. 1.

The threefold or C_3-symmetric paths in Fig. 2 are labeled by C_3-induced representations of icosahedral symmetry given in Table III. The most complicated cluster is the $K=99=0_3$ cluster belonging to the induced representation

$$0_3\uparrow I = A + T_1 + T_3 + 2G + H.$$

The $\pm 1_3\uparrow I$ clusters belong to $K=100$ and 98 have the same number (20) of base states but one fewer species:

$$1_3\uparrow I = T_1 + T_3 + G + 2H.$$

The $K=98$ cluster is below the cutoff K_3 value in (3.10) and is badly split in Fig. 1.

A theory of the ordering and relative spacing between species in clusters will be discussed in Sec. IV. It is interesting to note that the ordering of species without regard to spacing is uniformly the same throughout the entire manifold of $J=100$ in Fig. 1, and indeed, for any value of J. This makes it possible to replace the $R_3\supset I$ correlation Table I with a more elegant and informative level cluster wheel device which is shown in Fig. 3. The wheel gives the order and qualitative cluster form [in conjunction with cutoff formulas (3.10)] of all species in a $T^{[6]}$ spectrum for arbitrary integral J values. It is only necessary to calculate $(J)\mathrm{mod}(10)$ and $(J)\mathrm{mod}(6)$ and locate these numbers on the outside and inside arrows, respectively, of the wheel. The outside arrow indicates the beginning of the sequence starting from the highest level and points to which C_5 cluster that level belongs. The inside arrow does the same beginning with the lowest species in a C_3 level cluster. One needs to know the K-cutoff values [Eq. (3.10)] in order to predict where one kind of cluster "melts" into another, but the species ordering will be maintained throughout any J manifold for the spectrum of a sixth-rank $T^{[6]}$ tensor.

A complete rotation of the wheel occurs for $J=30$ and greater. The resulting set of $J=30$ species constitutes 60 levels plus a single A. The 60 levels are equivalent to the regular representation of I which is perhaps the grandest cluster of all. The regular representation is equivalent to the induced representation

$$D_1(\text{of } C_1)\uparrow I = A + 3T_1 + 3T_3 + 4G + 5H.$$

In Sec. V an RE surface and Hamiltonian involving mixed sixth- and tenth-rank tensors will be shown which gives this giant C_1 cluster. Related Hamiltonians which give the 30-fold degenerate C_2 clusters listed in Table III are shown there, too. These giant clusters also appear in the discussion of local vibrational modes.

Note that the wheel in Fig. 3 gives the correct ordering and clustering only for the eigenvalues of the sixth-rank tensor (2.1). For the mixed-rank tensor spectrum the fine

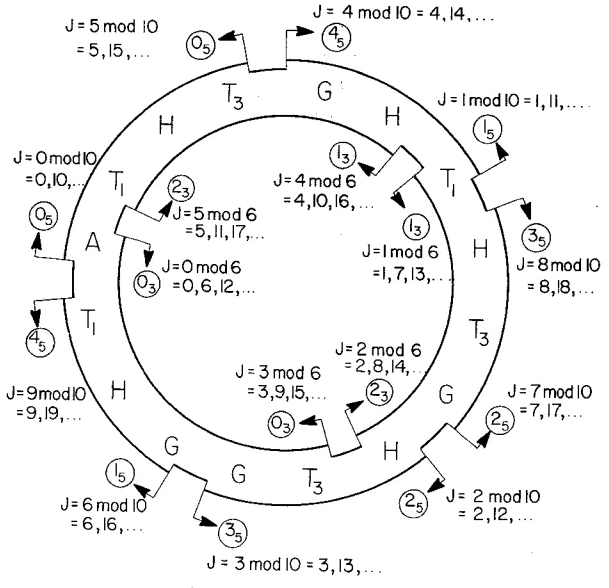

FIG. 3. Sequencing ring for icosahedral symmetry species in sixth-rank tensor spectrum for arbitrary angular momentum J. Ordering and clustering of species are indicated by segments of the ring as explained in the text. Note that the ordering or even J is opposite to that for odd J.

structure may have a completely different form as we will see in Sec. V. However, the same *number* of each species must appear regardless of the tensor rank.

IV. SUPERFINE STRUCTURE: QUANTITATIVE THEORY

The quantitative form of icosahedral superfine cluster splitting patterns can be determined in parametric form with the use of induced representation theory. The patterns which arise in the tensor splitting of clusters belonging to twofold, threefold, and fivefold local symmetries will be shown.

The analysis of a q-fold symmetry cluster begins with the development of an initial basis within which matrix elements of an effective Hamiltonian or tunneling operator may be deduced. This is accomplished with the construction of the left cosets of the local symmetry subgroup $C_q \in I$. Each coset is formed by multiplication of all $h \in C_q$ on the left-hand side by an arbitrarily chosen global symmetry operator $g \in I$. The process is repeated for each coset using a new $g' \in I$ where g' must not be an element of a coset previously formed. In this fashion all of the unique disjoint left cosets of $C_q \in I$ are obtained.

There is an isomorphism between each of the cosets of C_q and the initial basis vectors within which the tunneling operator may be expressed. The dimension d of this coset space is given by Lagrange's theorem where $d = {}^oI/{}^oC_q$. For $q = 5$ one has $d = 60/5 = 12$, and this corresponds to the fivefold clusters which contain 12 eigenvalues each. For $q = 3$ on has $d = 60/3 = 20$ which yields 20 eigenvalues in each C_3 cluster. Finally, $q = 2$ gives $d = 60/2 = 30$ for a total of 30 eigenvalues per twofold cluster.

The isomorphism between cosets and coset space basis vectors provides a convenient labeling scheme. Each basis vector is labeled by a representative group operator from each coset. By construction, the number of elements in each coset is the same as the number of elements in the subgroup C_q. This gives a choice of q labels for each basis vector.

A judicious choice of labeling operators l simplifies the calculation of the tunneling operator matrix elements. A representative operator or coset leader l is selected as a label if it maintains zero phase difference between adjacent portions of two q-fold symmetric wave functions where one is rotated from the other by the operator in question. Once the labeling operators are chosen the basis states are labeled by each operation on an initial basis vector $|1,n_q\rangle$. Each of the coset leaders gives

$$l\,|1,n_q\rangle = |l,n_q\rangle,$$

where n_q is the C_q irrep label that determines the specific type of C_q local symmetry of $|1,n_q\rangle$.

The 12 fivefold coset leaders are in one-to-one correspondence with the 12 fivefold symmetric hills on the T^6 RE surface. Similarly, the 20 threefold coset leaders correspond to the 20 valleys, and the 30 twofold coset leaders correspond to the 30 saddle points. With the establishment of this correspondence between coset leaders and RE surface topography it becomes possible to determine which coset leaders are nearest neighbors, next nearest neighbors, and so on. Matrix elements of the tunneling operator are given parametrically in this basis with H as the diagonal element, S as the nearest-neighbor tunneling amplitude, T as the next-nearest-neighbor tunneling amplitude and so on. By construction the resulting $q \times q$ matrix has icosahedral symmetry and is reducible to block diagonal form through symmetry analysis.

The key to implementing the symmetry analysis is the icosahedral projection operator

$$P^{\alpha}_{ij} = \frac{l^{\alpha}}{60} \sum_g D^{\alpha *}_{ij}(g)\, g, \tag{4.1}$$

where α is an icosahedral irrep label, l^{α} is the dimension of the αth irrep and the $D^{\alpha}_{ij}(g)$ are the (i,j)th elements of the αth irreducible representation (irrep) of $g \in I$. The indices i and j run from 1 to l^{α}. This means that the total number of projection operators is given by

$$60 = (l^{\alpha})^2 + (l^{T_1})^2 + (l^{T_3})^2 + (l^{G})^2 + (l^{H})^2.$$

In fivefold clusters, for example, a new basis is formed by the projection of an initial state $|1,n_5\rangle$ with the icosahedral projectors. The local symmetry of the state $|1,n_5\rangle$ is given by the C_5 irrep labels $n_5 = 0_5, 1_5, 2_5, 3_5$ or 4_5. The local state is affected by C_5 projection as follows:

$$P^{m_5}|1,n_5\rangle = P^{m_5}P^{n_5}|1\rangle/(N^{n_5})^{1/2} = |1,n_5\rangle\delta_{n_5 m_5}.$$

Here the P^{m_5} are the C_5 projectors

$$P^{m_5} = \frac{1}{5}\sum_{n=0}^{4} [D^{m_5}(h)^*]^n h^n \quad [D^{m_5}(h) = e^{2\pi i m/5}]$$

and N^{n_5} is a normalization factor. Note that indices i and j present in Eq. (4.1) are suppressed because the C_5 group is Abelian and $l^{\alpha} = 1$ for all α.

The projection of $|1,n_5\rangle$ by the icosahedral projectors will yield a set of basis states

$$P^{\alpha}_{i_5 j_5}|1,n_5\rangle/(N)^{1/2} = \left(\frac{l^{\alpha}}{12}\right)^{1/2} \sum_l D^{\alpha *}_{i_5 n_5}(l)\,|l,n_5\rangle\delta_{j_5 n_5}$$
$$= |i^{\alpha}_5 j_5 n_5\rangle\delta_{j_5 n_5}, \tag{4.2}$$

where the labels i_5 and j_5 of the icosahedral projector are C_5 irrep labels chosen in accord with the αth row of the C_5 correlation table (Table III) and the summation is over C_5 coset leaders l. The delta function in Eq. (4.2) allows only the expected number (12) of icosahedral projectors to yield a nonzero result. The C_5 irrep labeled columns of the C_5 correlation table indicate which of these projectors will work on the initial basis vector $|1,n_5\rangle$ with n_5-type C_5 local symmetry. The basis $\{|1,n_5\rangle\cdots|l,n_5\rangle\cdots\}$ spans what is called the (n_5) induced representation $(D^{n_5}\uparrow I)$. The vectors (4.2) span a reduced induced representation.

The representation of Hamiltonian in this basis (4.2) will be in block diagonal form with l^{α} identical blocks corresponding to each irrep α of I which appears in $D^{n_5}\uparrow I$.

For any C_5 coset space this form is completely diagonal since there are no repeated irreps in any column of the C_5 correlation table (3.2).

From (4.2) the eigenvalues of the tunneling Hamiltonian matrix follow.

$$\langle {}^{\alpha}_{i_5 j_5 n_5}|H|{}^{\beta}_{k_5 l_5 m_5}\rangle$$
$$= \sum_l D^{\alpha *}_{n_5 m_5}(l)\langle 1,n_5|H|1,m_5\rangle\delta^{\alpha\beta}\delta_{j_5 n_5}\delta_{l_5 m_5}\delta_{n_5 m_5}\delta_{i_5 k_5}. \tag{4.3}$$

Only the first row of the initial tunneling matrix is required. The eigenvalues that result from the $C_5\uparrow I$ analysis are shown in Fig. 4(a). Here the cluster center-of-gravity energy has been set to zero and superfine splitting has been expressed in terms of nearest-neighbor tunneling amplitude, S, only. The magnitude of the nearest-neighbor tunneling factor may, in principle, be calculated by a path integral along a single path on the RE surface that connects nearest-neighbor trajectories. It remains to be seen if one may determine next-nearest- or next-next-nearest-neighbor tunneling factors T or U, respectively, in the same fashion. The C_5 cluster splitting formulas in terms of these additional parameters are given in Table IV.

The C_3 and C_2 clusters are analyzed in the same fashion as the C_5 clusters. However, as the C_3 correlation table indicates there are two icosahedral $\alpha = G$ irreps in the 0_3 column and two $\alpha = H$ irreps in the 1_3 and 2_3 columns. Hence, the tunneling matrix in the 0_3, 1_3, and $2_3\uparrow I$ induced representations will contain α-labeled block diagonal elements with a dimension equal to the repeat frequency given in the correlation table. For the 0_2 and 1_2 induced representations there will be one three-dimensional and several two-dimensional blocks. The C_3 and C_2 cluster patterns are shown in Figs. 4(b) and 4(c) where, again, only nearest-neighbor tunneling is considered.

The results of the induced representation analysis may

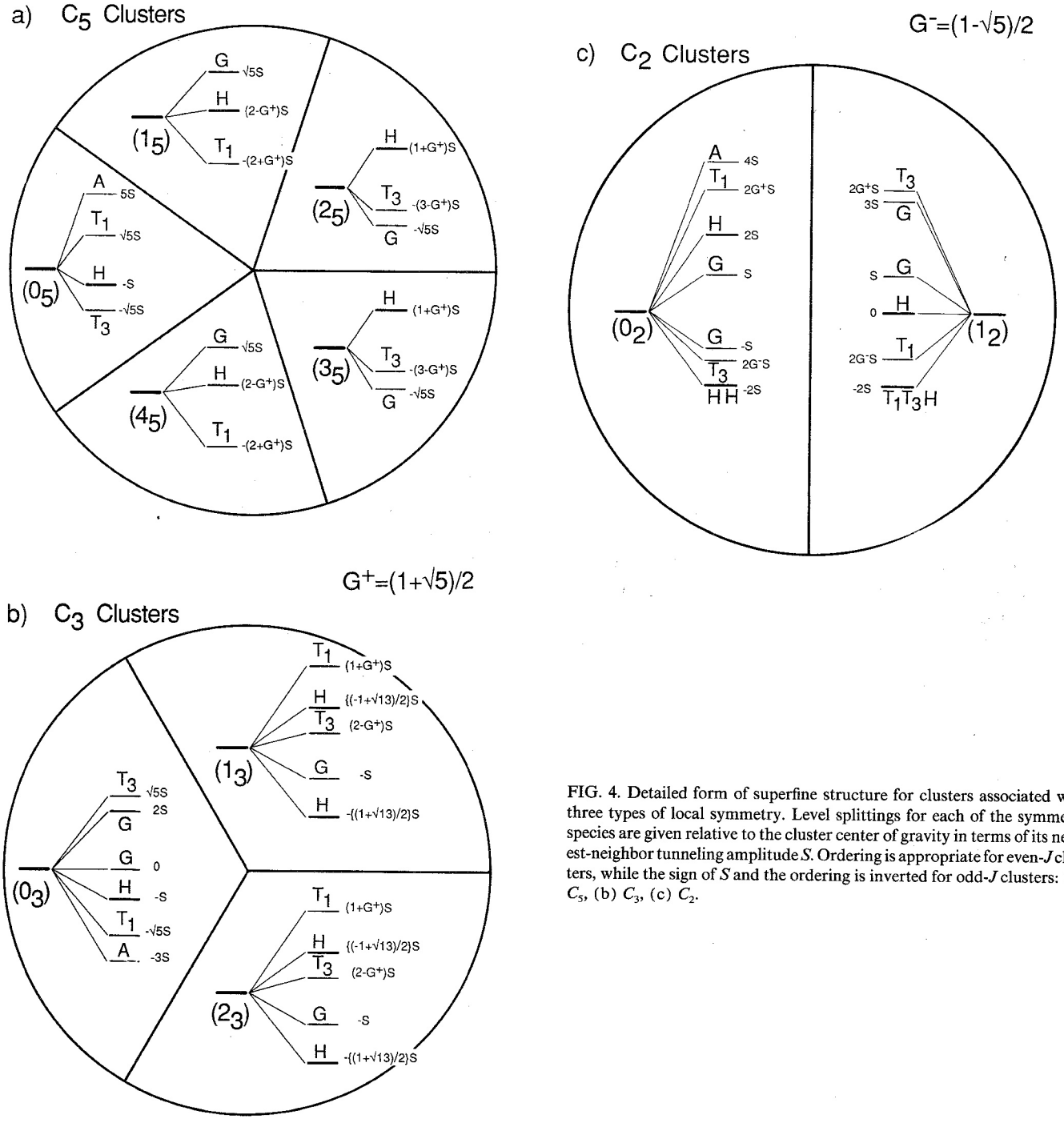

FIG. 4. Detailed form of superfine structure for clusters associated with three types of local symmetry. Level splittings for each of the symmetry species are given relative to the cluster center of gravity in terms of its nearest-neighbor tunneling amplitude S. Ordering is appropriate for even-J clusters, while the sign of S and the ordering is inverted for odd-J clusters: (a) C_5, (b) C_3, (c) C_2.

TABLE IV. Eigenvalue formulas for C_5 cluster superfine structure.

0_5 cluster eigenvalues	1_5 and 4_5 cluster eigenvalues	2_5 and 3_5 cluster eigenvalues
$E^A = H + 5S + 5T + U$	$E^{T1} = H - (2+G^+)S - (2+G^-)T$	$E^{T3} = H - (2+G^-)S - (2+G^+)T$
$E^{T1} = H + \sqrt{5}S - \sqrt{5}T - U$	$E^G = H + \sqrt{5}S - \sqrt{5}T$	$E^G = H - \sqrt{5}S + \sqrt{5}T$
$E^{T3} = H - \sqrt{5}S + \sqrt{5}T - U$	$E^H = H + (1+G^-)S + (1+G^+)T$	$E^H = H + (1+G^+)S + (1+G^-)T$
$E^H = H - S - T + U$		

be checked with those of an accurate numerical diagonalization of $T^{[6]}$ in a full $(2J+1)$-dimensional basis. One very sensitive test is a comparison of the ratio of differences between adjacent superfine levels. The 1_3 and 2_3 symmetries of the C_3 cluster family are particularly interesting since their nearest-neighbor tunneling formulas in Fig. 4(b) contain rather extraordinary expressions involving the radical $\sqrt{13}$. According to these formulas the ratio of adjacent differences are as follows:

$$\frac{T_1 - H}{H - T_3} = \frac{4 + \sqrt{5} - \sqrt{13}}{-4 + \sqrt{5} + \sqrt{13}} = 1.428\,371,$$

$$\frac{H - T_3}{T_3 - G} = \frac{-4 + \sqrt{5} + \sqrt{13}}{5 - \sqrt{5}} = 0.666\,304,$$

$$\frac{T_3 - G}{G - H} = \frac{5 - \sqrt{5}}{-1 + \sqrt{13}} = 1.060\,785.$$

The exact numerical values for the same ratios in a $K_3 = 205$ cluster of $J = 205$ agree to within five or six significant figures:

$$\frac{T_1 - H}{H - T_3} = 1.428\,364,$$

$$\frac{H - T_3}{T_3 - G} = 0.666\,302,$$

$$\frac{T_3 - G}{G - H} = 1.060\,778.$$

A comparison of 1_2 and 2_3 (C_3) cluster splitting ratios, predicted by induced representation theory and accurate numerical diagonalization for $J = 50$, 100, and 151, is given in Table V. The comparison improves steadily with increasing J.

V. MIXED SIXTH- AND TENTH-RANK ICOSAHEDRAL EIGENSOLUTIONS

The RE surface geometry will now be used to predict and analyze the eigensolutions of a mixed-tensor operator:

TABLE V. C_3 cluster superfine splitting ratios.

	Induced representation	Accurate numerical values		
		$J = 50$	$J = 100$	$J = 151$
$\frac{T_1 - H}{H - T_3} =$	1.428 371	1.678 ...	1.440 1..	1.428 002
$\frac{H - T_3}{T_3 - G} =$	0.666 304	0.905 ...	0.666 6..	0.666 275
$\frac{T_3 - G}{G - H} =$	1.060 785	0.987 ...	1.078 2..	1.060 257

$$H(\nu) = B|J|^2 + (\cos\nu)T^{[6]} + (\sin\nu)T^{[10]}. \quad (5.1)$$

Here the angle ν is used to artificially vary the coefficient $(\cos\nu)$ of the sixth-rank tensor $T^{[6]}$ [Eq. (2.1)] and the coefficient $(\sin\nu)$ of the tenth-rank tensor $T^{[10]}$ [Eq. (2.2)] while maintaining unit normalization overall. In a "real" Hamiltonian these coefficients would vary according to different powers or polynomials of the angular momentum J as explained in Sec. II. An example of tetrahedral fourth- and sixth-rank tensor admixtures have been studied and used in a qualitative comparison of some methane (CH_4) fine structure.[27]

The addition of even relatively small amounts of the tenth-rank tensor radically alters the form of the RE surface as shown in the computer graphics of Fig. 5. Each figure is labeled by ν in units of $\pi/6$. One can visualize tensor mixtures with different ν values according to hours on an imaginary clock; 12 o'clock or $\nu = 0$ is pure sixth-rank tensor $T^{[6]}$, 1:30 o'clock or $\nu = 1.5$ $(\pi/6)$ is equal to amounts of $T^{[6]}$ and $T^{[10]}$, 3 o'clock or $\nu = 3(\pi/6)$ is pure tenth-rank tensor $T^{[10]}$, and 6 o'clock or $\nu = \pi$ is pure *negative* sixth-rank tensor $-T^{[6]}$. The values of ν included in Fig. 5 are (a) $\nu = 0.0$, (b) $\nu = 0.3\pi/6$, (c) $\nu = 1.0\pi/6$, (d) $\nu = 2.0\pi/6$, (e) $\nu = 3.0\pi/6$, (f) $\nu = 4.0\pi/6$, (g) $\nu = 4.1\pi/6$, and (h) $\nu = 5.0\pi/6$. All contour paths are drawn as 21 equally spaced levels and are therefore *not* precisely quantizing trajectories for any particular value of J. The density of paths is roughly that of $J = 150$.

Each tensor mixture and its corresponding RE surface in Fig. 5 describes a different set of eigensolutions for a given J. The $J = 100$ eigenvalues are plotted as a function of ν in Fig. 6. The eigenvalue plot is marked with letters (a) to (h) at the ν values which are represented by RE surfaces in Fig. 5(a)–5(h), respectively. Point (a) corresponds to the $\nu = 0$ surface in Fig. 5(a) which is a copy of Fig. 2. The levels above point (a) on the extreme left-hand side of Fig. 6 are proportional to the ones shown in Fig. 1.

At point (b) in Fig. 6 a remarkable rearrangement of levels occurs in the lower portion of the spectrum. This corresponds to the $\nu = 0.3(\pi/6)$ RE surface in Fig. 5(b) in which the C_3 paths of the previous figure (a) have vanished and been replaced by more C_5 paths. This is consitent with the (b) spectrum in Fig. 6 which is composed almost entirely of levels belonging to C_5 clusters. The undecided (GH) pair near the separatrix in Fig. 1 picks up a T_1 level from the C_3 $(K_3 = 98)$ cluster just below it to make a $(GHT_1) - (K_5 = 89)$ C_5 cluster at the (b) point in Fig. 6. The rest of the C_3 $(K_3 = 98)$ cluster forms two $(HT_3G)(K_5 = 88, 87)$ clusters with some help from the $(K_3 = 99)$ cluster. The remaining levels form a disorganized

a) $\upsilon = 0.0$

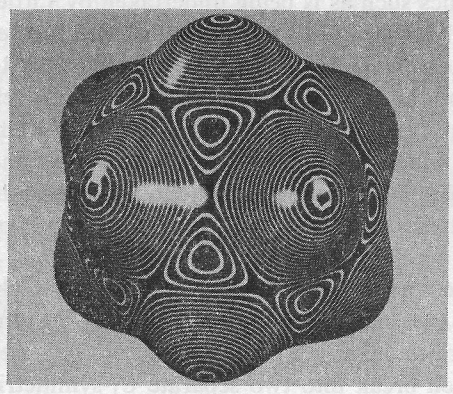

b) $\upsilon = 0.3\pi/6$

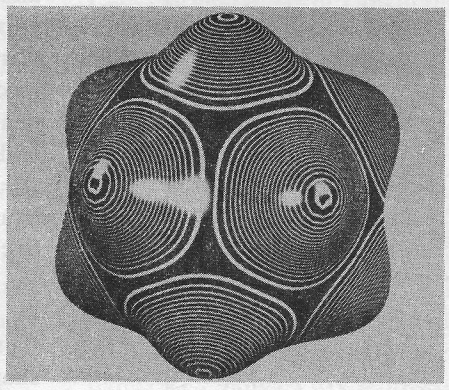

c) $\upsilon = 1.0\pi/6$

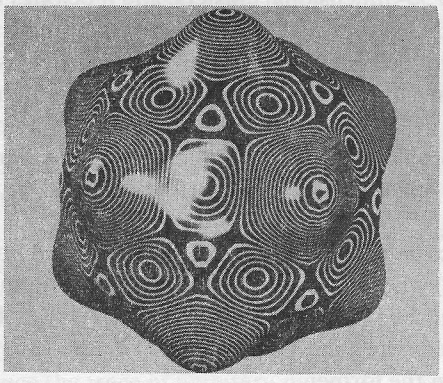

d) $\upsilon = 2.0\pi/6$

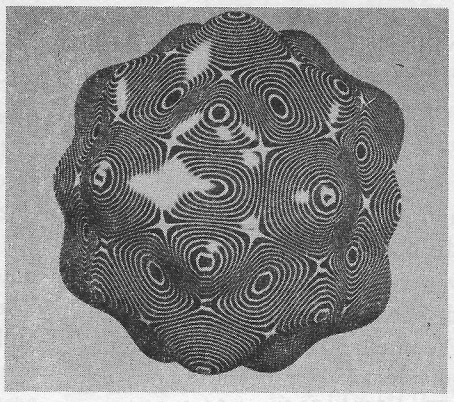

FIG. 5. Rotational energy surfaces and level curves for varying mixtures of sixth- and tenth-rank icosahedral tensor Hamiltonians. $T^{(6)} \cos \nu + T^{(10)} \sin \nu$: (a) $\nu = 0.0\pi/6$; (b) $\nu = 0.3\pi/6$; (c) $\nu = 1.0\pi/6$; (d) $\nu = 2.0\pi/6$; (e) $\nu = 3.0\pi/6$; (f) $\nu = 4.0\pi/6$; (g) $\nu = 4.1\pi/6$; (h) $\nu = 5.0\pi/6$.

e) $\upsilon = 3.0\pi/6$

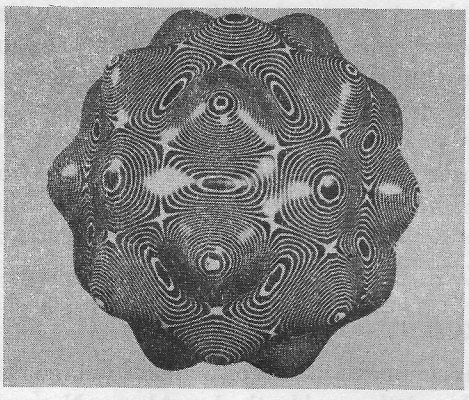

f) $\upsilon = 4.0\pi/6$

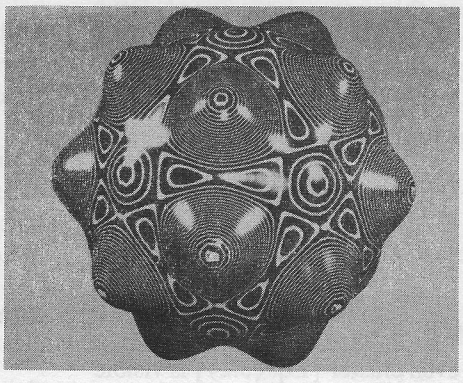

g) $\upsilon = 4.1\pi/6$

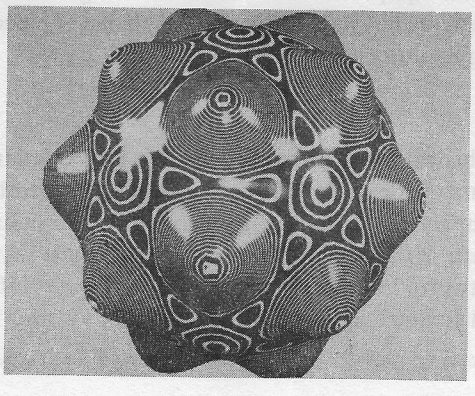

h) $\upsilon = 5.0\pi/6$

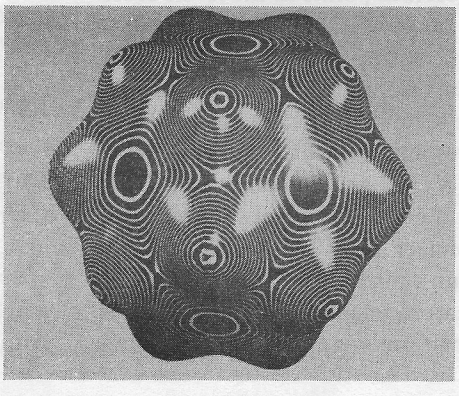

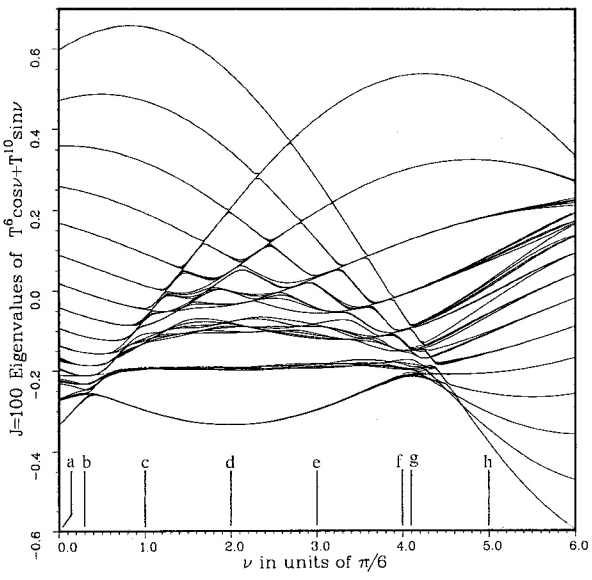

FIG. 6. $J = 100$ eigenvalues for varying mixtures of sixth- and tenth-rank icosahedral tensor Hamiltonians. Points corresponding to RE surfaces in Figs. 5(a)–5(h) are indicated.

combination of (GHT_1) and (AT_1HT_3) clusters with a G and an H level hidden at the bottom.

By the next step (c) ($\nu = \pi/6$) a completely new type of cluster has been established. The two lowest clusters of levels for points (c), (d), and (e) contain 30 levels each. The each correspond to a set of 30 equivalent C_2 symmetric quantizing paths on the RE surface in Figs. 5(c), 5(d), or 5(e), respectively. Recall that the level paths in Fig. 5 are drawn according to an arbitrary but equal spacing between maximum and minimum RE values. Since they are not quantized paths they cannot be identified one-to-one with C_2 clusters.

Each of the 30-state C_2 clusters in Fig. 5 contain I species predicted by Table III and Fig. 4. The lowest ($K_2 = 100$) cluster belongs to the even induced representation

$$0_2\uparrow I \sim A + T_1 + T_3 + 2G + 3H, \tag{5.2}$$

while the next ($K_2 = 99$) cluster belongs to the odd induced representation

$$1_2\uparrow I \sim 2T_1 + 2T_3 + 2G + 2H. \tag{5.3}$$

The "remains" of another even cluster [Eq. (5.2)] is visible in Fig. 6 above the two lowest clusters between $\nu = 1.0(\pi/6)$ and $\nu = 4.0(\pi/6)$. The eight species of levels are clearly visible in this configuration at various points as the levels cross and uncross.

Similar crossing and uncrossing is occurring inside the lower two C_2 clusters. At the resolution of Fig. 6 this is only barely visible in parts of the second ($K_2 = 99$) cluster, but a 10- or 20-fold increase in resolution would reveal the same phenomena in the lowest ($K_2 = 100$) cluster, as well. This crossing is a manifestation of competition between effective tunneling paths which connect the C_2 domains in Figs. 5(c)–5(f). There are certain ranges of ν values where the splitting pattern due to nearest-neighbor-only tunneling is well approximated. These patterns were shown in Fig. 4 and the $K_2 = 98$ pattern around $\nu = 1.5(\pi/6)$ is approximated by the 0_2 pattern in Fig. 4. A detailed analysis of tunneling and wave dynamics such as is being undertaken by Littlejohn *et al.*,[26] and Huber *et al.*[25] will be needed to further clarify this phenomenon. Also, it would be interesting to study the eigensolutions in the neighborhoods of the "accidental" or "Fermi resonant" crossings between C_3 clusters and C_5 clusters which occur between $\nu = 1.0(\pi/6)$ and $\nu = 4.0(\pi/6)$ in Fig. 6. Here there is tunneling between nonequivalent trajectories on hills of different symmetry in Figs. 5(c)–5(f).

Finally, there is a remarkable C_2 to C_1 symmetry breaking around $\nu = 4.0(\pi/6)$. As seen in Figs. 5(f) and 5(g) the C_2-symmetric trajectories get squeezed into "bow-tie" shapes which each break into two separate C_1-symmetric valleys. This yields a giant 60-dimensional cluster at the low end of the $\nu = 4.1(\pi/6)$ spectrum in Fig. 6. The giant is formed out of two 30-dimensional clusters, and it belongs to the regular C_1-induced representation mentioned at the end of Sec. III. The two-well potential or the two-level system is a paradigm of quantum theory of spontaneous symmetry breaking. At $\nu = 4.1(\pi/6)$ one has the icosahedral version of the two-well problem. At much higher J with the same resolution as Fig. 6 one will only see two levels merging into one at this point.

The difference between Fig. 5(b) where C_5 paths dominate and Fig. 5(g) where C_3 paths dominate is worth noting. The latter has a more complicated separatrix geometry in the valleys which yields the giant C_1 clusters, while the valleys are "smoother" in the former.

VI. CONCLUSION

Semiclassical and graphical methods have been described for approximating and visualizing rotational and rovibrational eigensolutions for molecules having icosahedral symmetry. These methods provide simple ways to analyze the eigenvectors as well as the eigenvalues of a variety of complicated tensor Hamiltonians having icosahedral symmetry. These methods allow one to predict the forms and patterns of fine structure that might arise in laser spectra of molecules described by icosahedral tensor Hamiltonians.

ACKNOWLEDGMENTS

This work is supported in part by a grant from the National Science Foundation and by the Los Alamos National Laboratory through a grant from the Department of the Army. Graphical equipment used in the later stages of this project were provided by a grant from the Arkansas Science and Technology Authority (ASTA).

APPENDIX A

The icosahedral point group $I[I_h = I \times (i)]$ contains 60 {120} symmetry operations. These may be classified by the rotation angle ω of each operator around its symmetry axis. There are 20 threefold symmetric rotations with $\omega = 120°$, 15 twofold symmetric rotations with $\omega = 180°$, and 24 fivefold symmetric rotations, 12 with $\omega = 72°$ and 12 with $\omega = 144°$.

These disjoint sets of operators form the class structure of the icosahedral group I. The unit operator with $\omega = 0$ is the only element in the class C_1. The 12 fivefold symmetric rotations with $\omega = 72°$ form the class C_R. The 12 fivefold symmetric rotations with $\omega = 144°$ form the class C_{R^2}. The 20 threefold symmetric rotations form the class C_i. Elements in a class may be transformed into one another by a similarity transformation by at least one element of the group I.

The classes of I_h are obtained from those of I by operating on the elements of the classes of I with the elements of the inversion group $C_{IN} = \{1, IN\}$ where IN is the inversion operator. Multiplication with the unit operator duplicates the classes of I while multiplication with IN creates five new classes for a total of ten I_h classes,

$$1C_1 = C_1, \quad INC_1 + C_{I1},$$
$$1C_R = C_R, \quad INC_R = C_{IR},$$
$$1C_{R^2} = C_{R^2}, \quad INC_{R^2} = C_{IR^2},$$
$$1C_r = C_r, \quad INC_r = C_{Ir},$$
$$1C_i = C_i, \quad INC_i = C_{Ii}.$$

The I_h character table is given in (a) of Table VI. The columns are labeled by class and the rows are labeled by I_h irrep labels α. Each entry in a given row α is the trace of the I_h irrep $D^{\alpha}_{(g)}$ of any operator g in the class that labels the column of the selected entry

$$X^{\alpha}_{(g)} = \text{Trace}(D^{\alpha}_{g}) = \sum_i D^{\alpha}_{ii}(g).$$

Since the trace of a unitary matrix is independent of a similarity transformation and by definition elements in the same class may be transformed into one another one would expect that all of the irreps of the elements in the same class have the same trace. The subscript g and a stand for the German words *gerade* and *ungerade*, meaning even and odd, respectively. These label the parity of the eigenfunctions associated with α-labeled eigenvlues.

The characters of I_h are obtained from those of I by the cross product of the characters of I and the characters of C_{IN}. The characters of I are in the upper left-hand corner of Table VI. The characters of C_{IN} are given in (b) of Table VI. The cross product of I with C_{IN} multiplies the characters of I with 1 three times and -1 once. This yields the four sets of I characters with the one in the lower right-hand corner, the negative of the others.

In many cases the use of group characters in the solution of a problem greatly reduces the amount of analysis required in that the group irreps are not needed. Here we reproduce the 0_5 cluster eigenvalues given in Table IV using icosahedral characters only. The exact reproduction of the formulas given is possible because there are no repeated irreps in the reduced C_5 induced to I representation.

Eigenvalues are given by

$$E^{\alpha} = \left(\frac{1}{{}^{o}G}\right) \sum_{\substack{\text{classes} \\ C_g}} X^{\alpha *}_{(g)}\, {}^{o}C_g \text{ Trace } \langle Hg \rangle, \tag{A1}$$

where $X^{\alpha}_{(g)}$ is the αth character of g given in (a) of Table VI. The order of the class C_g is denoted ${}^{o}C_g$, H is the $C_5 \uparrow I$ tunneling Hamiltonian and the element g is a representative operator arbitrarily chosen from the class C_g. The trace is given by

$$\text{Trace } \langle Hg \rangle = \sum_l \langle ln_5 | Hg | ln_5 \rangle \tag{A2a}$$
$$= \sum_l \langle 1n_5 | l^{-1} H | gln_5 \rangle$$
$$= \sum_l \langle 1n_5 | H | l^{-1} gln_5 \rangle, \tag{A2b}$$

where the commutation of the Hamiltonian H and the C_5 coset leaders l was used, and $n_5 = 0_5, 1_5, 2_5, 3_5$, and 4_5 are C_5 irrep labels. The trace given by Eq. (A2b) is particularly useful in that it requires only the first row of the $C_5 \uparrow I$ tunneling matrix.

TABLE VI. (a) Characters of the icosahedral group. (b) Characters of the inversion group.

(a)

	C_1	C_R	C_{R^2}	C_r	C_i	C_{I1}	C_{IR}	C_{IR^2}	C_{Ir}	C_{Ii}
A_g	1	1	1	1	1	1	1	1	1	1
T_{1g}	3	G^+	G^-	0	-1	3	G^+	G^-	0	-1
T_{3g}	3	G^-	G^+	0	-1	3	G^-	G^+	0	-1
G_g	4	-1	-1	1	0	4	-1	-1	1	0
H_g	5	0	0	-1	1	5	0	0	-1	1
A_u	1	1	1	1	1	-1	-1	-1	-1	-1
T_{1u}	3	G^+	G^-	0	-1	-3	$-G^+$	$-G^-$	0	1
T_{3u}	3	G^-	G^+	0	-1	-3	$-G^-$	$-G^+$	0	1
G_u	4	-1	-1	1	0	-4	1	1	-1	0
H_u	5	0	0	-1	1	-5	0	0	1	-1

$G^+ = (1+\sqrt{5})/2$ $\qquad$ $G^- = (1-\sqrt{5})/2$

(b)

	C_i	C_{IN}
+	1	1
−	1	−1

Substitution of Eq. (A2b) into Eq. (A1) yields

$$E^{\alpha}=\left(\frac{1}{{}^{o}G}\right)\sum_{\substack{\text{classes}\\ C_g}}\sum_{l}X^{\alpha *}_{(g)}\,{}^{o}C_g\langle 1n_5|H|l^{-1}gln_5\rangle. \quad \text{(A3)}$$

It is important to note that the product $l^{-1}gl$ will in general belong to a C_5 coset but it may not be the leader chosen for the C_5 induced representation. The result is that for $n_5=1_5$, 2_5, 3_5, and 4_5 the matrix element $\langle 1n_5|H|l^{-1}gln_5\rangle$ will be shifted by a phase factor dependent on $l^{-1}gl$. However, for $n_5=0_5$ the matrix elements are independent of the choice of coset leader and Eq. (A3) may be used with the initial tunneling matrix elements derived in Sec. IV.

Evaluation of the matrix elements $\langle 1n_5|H|l^{-1}gln_5\rangle$ in Eq. (A3) gives

$$\begin{aligned}E^{\alpha}=\tfrac{1}{60}\big[&X^{\alpha *}_{C_1}+2X^{\alpha *}_{C_R}+2X^{\alpha *}_{C_{R^2}})12H\\&+(2X^{\alpha *}_{C_R}+2X^{\alpha *}_{C_r}+X^{\alpha *}_{C_i})60S\\&+(2X^{\alpha *}_{C_{R^2}}+2X^{\alpha *}_{C_r}+X^{\alpha *}_{C_i})60T\\&+X^{\alpha *}_{C_i}60U\big]. \end{aligned}\quad \text{(A4)}$$

Substitution of the characters $X^{\alpha}_{c_g}$ from (a) of Table VI into Eq. (A4) results in the following expressions for the 0_5 cluster eigenvalues

$$\begin{aligned}E^{A}&=\tfrac{1}{60}[(1+2+2)12H+(2+2+1)60S\\&\quad+(2+2+1)60T+60U]\\&=H+5S+5T+U,\\E^{T_1}&=\tfrac{1}{60}[(3+2G^{+}+2G^{-})12H+(2G^{+}-1)60S\\&\quad+(2G^{-}-1)60T-60U]\\&=H+\sqrt{5}S-\sqrt{5}T-U,\\E^{T_2}&=\tfrac{1}{60}[(3+2G^{-}+2G^{+})12H+(2G^{-}-1)60S\\&\quad+(2G^{+}-1)60T-60U]\\&=H-\sqrt{5}S+\sqrt{5}T-U,\\E^{H}&=\tfrac{1}{60}[(5)12H+(-2+1)60S\\&\quad+(-2+1)60T+60U]\\&=H-S-T+U.\end{aligned}$$

The evaluation of Eq. (A4) with $\alpha=G$ characters yields

$$E^{G}=0.$$

In order to calculate the $n_5=1_5$, 2_5, 3_5, and 4_5 cluster splittings using the tunneling matrix derived in Sec. IV the use of icosahedral irreps is necessary. Methods for generating these irreps will be given in the following paper.

APPENDIX B

Diagonalization of a tensor operator T is greatly facilitated through the use of its symmetry. If g is an element of a group G of order ${}^{o}G$ and $gT=Tg$ for all $g\in G$, then T has G symmetry. Analysis of the group G yields the irreducible representations (irreps) which permit the explicit construction of the group projection operators. These are given by the expansion

$$P^{\alpha}_{ij}=\left(\frac{l^{\alpha}}{{}^{o}G}\right)\sum_{g}D^{\alpha *}_{ij}(g)g, \quad \text{(B1)}$$

where l^{α} is the dimension of the αth irrep, $g\in G$, and $D^{\alpha}_{ij}(g)$ is the i,j component of the αth irrep of g.

The projection of the angular momentum basis $|^{J}_{M}\rangle$ with P^{α}_{ij} yields a nonorthogonal basis within which the tensor operator T is block diagonal,

$$\begin{aligned}|^{J\alpha}_{mi_qj_q}\rangle&=P^{\alpha}_{i_qj_q}|^{J}_{m}\rangle\\&=\left(\frac{l^{\alpha}\,{}^{o}H}{{}^{o}G}\right)\sum_{l}\sum_{m'}D^{\alpha *}_{i_qj_q}(l)^{J}_{m'm}(l)|^{J}_{m'}\rangle\delta_{i_qm_q}.\end{aligned}\quad \text{(B2)}$$

Equation (B2) is obtained by the use of the expansion (B1) and the transformation properties of the $|^{J}_{m}\rangle$,

$$g|^{J}_{m}\rangle=\sum_{J'}\sum_{m'}|^{J'}_{m'}\rangle\langle^{J'}_{M'}|g|^{J}_{m}\rangle=\sum_{m'}{}^{J}_{m'm}(g)|^{J}_{m'}\rangle, \quad \text{(B3)}$$

where the $D^{J}_{m'm}(g)$ are the m', m components of the $JR3$ irrep. The summation over all $g\in G$ is reduced to a summation over the coset leaders of an Abelian group $H\subset G$ via coset factorization. Usually, H is a cyclic group C_q. The notation i_q in (B2) means i mod q and labels the irrep of C_q and the type of local symmetry that a wave function $\langle\theta,0|^{J}_{m}\rangle$ has about an axis colinear with the symmetry axis of C_q. The δ function in (B2) demonstrates that many projection operators will map the basis vector $|^{J}_{m}\rangle$ into a null vector. These null projections may be avoided through the use of the rotational correlation wheel in Fig. 3. Starting with the appropriate angular momentum and working around the wheel the correct group irrep lable may be selected. The projection operator label j_q is given by K which begins at $K=J$ and decreases by one unit for each cluster that is used. In this fashion each m value may be used as an orbit label and the projection operators of the group G may be used repeatedly. The frequency that a given irrep label is encountered as the wheel is traversed is the dimension of the resulting block diagonal element of the tensor operator labeled by the irrep label α. A reasonable estimate of the dimension of any labeled block is given by

$$d^{\alpha}\simeq\frac{(2J+1)l^{\alpha}}{{}^{o}G}. \quad \text{(B4)}$$

The frequency of any α labeled block is 1^{α} and reflects the degeneracy inherent in the symmetry of T. Each one of the l^{α} block elements is labeled by a different i_q in Eq. (A5) where the range of i_q is from 1 to l^{α}.

In the projected basis the tensor operator T has the form

$$\begin{aligned}T^{\alpha}_{mn}&=\langle^{J\alpha}_{mi_qm_q}|T|^{J\alpha}_{hi_qn_q}\rangle\\&=\left(\frac{l^{\alpha}\,{}^{o}H}{{}^{o}G}\right)\sum_{l}\sum_{m'}{}^{\alpha *}_{Dm_qn_q}(l)^{J}_{D_{m'n}}(l)\langle^{J}_{m}|T|^{J}_{m'}\rangle.\end{aligned}\quad \text{(B5)}$$

The summation over m' is limited by the constraint that $m1+m2=m3$ in the coupling coefficient $C^{rJJ}_{qK'K}$ used by the Wigner Ekhart theorem to evaluate the matrix element

$$\left\langle\begin{matrix}J\\m\\K\end{matrix}\middle|T^{r}_{q}\middle|\begin{matrix}J\\m'\\K'\end{matrix}\right\rangle.$$

Since the projected basis is nonorthogonal a generalized

eigenvalue problem must be solved. This requires the construction of an overlap matrix S whose elements are scalar products of the projected basis vectors with themselves:

$$S^{\alpha}_{mn} = \langle {}^{J\alpha}_{mi_q m_q} | {}^{J\alpha}_{ni_q n_q} \rangle = \left(\frac{l^{\alpha\, o}H}{{}^{o}G} \right) \sum_{l} D^{\alpha *}_{m_q n_q}(l) D^{J}_{mn}(l). \tag{B6}$$

For the case of an orthonormal set of basis vectors S becomes the unit operator.

Both the T^{α}_{mn} and S^{α}_{mn} are used to construct the αth eigenvalue equation:

$$\{T - \lambda S\}|\psi\rangle = 0.$$

This is solved by first transforming S into the unit operator while operating on T with the same transformations. The matrix T is then diagonalized in the usual fashion. There are also standard computer routines designed to find the eigenvalues of T given T and S. The resulting eigenvalues will be symmetry labeled by the irreps of the group G. Since the expressions in (B5) and (B6) are independent of i_q only one of the α blocks needs to be diagonalized.

For the icosahedral group, the sixth-rank icosahedral tensor, and $J = 100$ it is necessary to diagonalize a 201×201 matrix to find the eigenvalues of the tensor if symmetry projection is not invoked. With projection one 4×4, two 10×10, one 13×13, and one 17×17 matrix are all that need diagonalization. For $J = 1000$ projection requires the diagonalization of at most a matrix of dimension 175. Since the projection metod also labels eigenvalues by symmetry this avoids the symmetry labeling problems inherent in the nonprojective method.

[1] J. A. Wunderlich and W. N. Lipscomb, J. Am. Chem. Soc. **82**, 4427 (1960).

[2] C. L. Beckel and James P. Vaughan, in *Boron-Rich Solids*, edited by D. Emin, T. Aselage, C. L. Beckel, I. A. Howard, and C. Wood (AIP Conf. Proc. No. 140) (AIP, New York, 1985).

[3] L. A. Paquette, R. J. Ternasky, D. W. Balough, and G. Kentgas, J. Am. Chem. Soc. **105**, 5446 (1983).

[4] H. W. Kroto, J. R. Heath, S. C. O'Brien, R. F. Curl, and R. E. Smalley, Nature **318**, 162 (1985).

[5] M. Luo, G. Vriend, G. Kamer, I. Minor, E. Arnold, M. G. Rossmann, V. Boege, D. G. Scraba, G. M. Duke, and A. C. Palmenberg, Science **235**, 182 (1987).

[6] J. Hogle, M. Chow, and D. Filman, Sci. Am. **256**, 42 (1987).

[7] F. Doane and N. Anderson, *Electron Microscopy in Diagnostic Virology* (Cambridge University Press, Cambridge, England, 1987), p. 51.

[8] D. S. Shectman, I. Blech, D. Gratias, and J. W. Cahn, Phys. Rev. Lett. **53**, 1951 (1984); J. E. S. Socolar and P. J. Steinhardt, Phys. Rev. B **34**, 617 (1986).

[9] M. Hammermesh, *Group Theory and its Application to Physical Problems* (Addison-Wesley, Reading, MA, 1972), p. 51.

[10] K. T. Hecht, J. Mol. Spectrosc. **5**, 355 (1960).

[11] K. R. Lea, M. J. M. Leask, and W. P. Wolf, J. Phys. Chem. Solids **23**, 1381 (1962).

[12] A. J. Dorney and J. K. G. Watson, J. Mol. Spectrosc. **42**, 1 (1972).

[13] K. Fox, H. W. Galbraith, B. J. Krohn, and J. D. Louck, Phys. Rev. A **15**, 1363 (1977).

[14] (a) W. G. Harter and C. W. Patterson, Phys. Rev. Lett. **38**, 224 (1977); (b) J. Chem. Phys. **66**, 4872 (1977); (c) Int. J. Quantum Chem. Symp. **11**, 479 (1977); (d) Phys. Rev. A **19**, 2277 (1979); (e) J. Chem. Phys. **80**, 4241 (1984).

[15] C. W. Patterson and W. G. Harter, J. Chem. Phys. **66**, 4886 (1977).

[16] W. G. Harter, C. W. Patterson, and F. J. da Paixao, Rev. Mod. Phys. **50**, 37 (1978).

[17] W. G. Harter, Phys. Rev. A **2**, 192 (1981).

[18] W. G. Harter, J. Stat. Phys. **36**, 749 (1984).

[19] W. G. Harter and D. E. Weeks, Chem. Phys. Lett. **132**, 387 (1986).

[20] A. S. Pine, A. G. Maki, A. G. Robiette, B. J. Krohn, J. K. G. Watson, and Th. Urbanek, J. Am. Chem. Soc. **106**, 891 (1984).

[21] J. Raynal, J. Math. Phys. **25**, 1187 (1984).

[22] W. G. Harter, C. W. Patterson, and H. W. Galbraith, J. Chem. Phys. **69**, 4896 (1978).

[23] K. Fox, J. Mol. Spectrosc. **7**, 207 (1965).

[24] A. R. Edmonds, *Angular Momentum in Quantum Mechanics* (Princeton University Press, Princeton, N.J., 1957), p. 122.

[25] D. Huber, E. J. Heller, and W. G. Harter, J. Chem. Phys. **87**, 1116 (1987).

[26] R. G. Littlejohn, Phys. Rep. **138**, 193 (1986).

[27] W. G. Harter and C. W. Patterson, J. Math. Phys. **20**, 1453 (1979).